Research Article Vol. 34, No. 4 / April 2017 / Journal of the Optical Society of America B 785

Journal of the Optical Society of America B

OPTICAL PHYSICS

Nonlinear frequency combs generated by cnoidal waves in microring resonators

Zhen Qi,[1,*] Giuseppe D'Aguanno,[1,2] and Curtis R. Menyuk[1]

[1]Department of Computer Science and Electrical Engineering, University of Maryland at Baltimore County, 1000 Hilltop Circle, Baltimore, Maryland 21250, USA
[2]Department of Electrical and Computer Engineering, University of Texas at Austin, Austin, Texas 78712, USA
*Corresponding author: zhenqi1@umbc.edu

Received 26 December 2016; revised 20 February 2017; accepted 21 February 2017; posted 21 February 2017 (Doc. ID 283615); published 10 March 2017

Cnoidal waves are the periodic analog of solitons. Like solitons, they can be generated in microresonators and correspond to frequency combs. The generation of frequency combs in nonlinear microresonators is modeled by the Lugiato–Lefever equation. In this paper, we study the Lugiato–Lefever equation for a microresonator in the anomalous dispersion regime. In the lossless case, we show that the cnoidal waves can be expressed as a combination of Jacobi elliptic functions. These solutions reduce to known soliton-like solutions in particular cases. The properties of cnoidal waves in the realistic lossy case and their potential uses are also discussed.

OCIS codes: (190.4380) Nonlinear optics, four-wave mixing; (140.4780) Optical resonators; (190.3270) Kerr effect.

https://doi.org/10.1364/JOSAB.34.000785

1. INTRODUCTION

Octave-spanning (broadband) combs that are generated in externally pumped, high-quality (Q) microresonators with a Kerr nonlinearity have important potential applications to metrology, high-resolution spectroscopy, and microwave photonics [1–7]. However, narrowband combs also have important potential applications that include the nonlinear generation of new frequencies [8], quantum networking [9], and astrocombs [10]. Soliton generation appears at present to be the best path toward achieving an octave-spanning comb [1,5]. However, solitons are not always easy to obtain, and it has been found computationally that periodic solutions will often appear instead in a microresonator [11,12]. Thus, it is important to understand the circumstances under which these periodic solutions appear and whether they can be used to create a broadband comb.

The generation of frequency combs in a nonlinear microresonator is governed by the Lugiato–Levefer equation (LLE) [4,11–17]. Periodic solutions called Turing rolls have been experimentally observed [3] and computationally studied [12] in microresonators. However, the relationship of these solutions to solitons has been unclear. Our paper aims at filling this gap.

The LLE has analytical soliton solution when loss is neglected. While analytical solutions no longer exist when loss is included, these solutions still have great value since the soliton solutions in the presence of loss, sometimes referred to as dissipative solitons, closely resemble their lossless counterparts. Moreover, the analytical relationships among the soliton amplitude, duration, and pedestal size have been a useful guide to experiments and a useful starting point for computational and perturbative studies. It is reasonable to anticipate that the periodic solutions of the lossless LLE will be similarly useful.

In this work, we study the cnoidal wave solutions of the LLE in the anomalous dispersion regime of a microresonator, which are the periodic generalization of the soliton solutions. We show that the family of solutions that includes solitons and Turing rolls can all be represented analytically as Jacobi elliptic functions [18] when loss is neglected. These cnoidal wave solutions come in two generic forms, corresponding to two different types of Jacobi elliptic functions [$\mathrm{dn}(x|k^2)$, $\mathrm{cn}(x|k^2)$], where k is the modulus of these functions. The modulus k determines how rapidly the Fourier spectrum of these functions falls off. For Jacobi elliptic functions, when $k \to 0$, $\mathrm{dn}(x|k^2) \to 1$, $\mathrm{cn}(x|k^2) \to \cos(x)$, and $\mathrm{sn}(x|k^2) \to \sin(x)$; when $k \to 1$, $\mathrm{dn}(x|k^2) \to \mathrm{sech}(x)$, $\mathrm{cn}(x|k^2) \to \mathrm{sech}(x)$, and $\mathrm{sn}(x|k^2) \to \tanh(x)$. For the LLE, when $k \to 1$, the cnoidal wave solutions reduce to the soliton solutions that Matsko *et al.* [13] found. The period of the cnoidal waves is given by $4K(k)$, where $K(k)$ is a complete elliptic integral of the first kind [18]. We have $K(k) \to \pi/2$ as $k \to 0$ and $K(k) \to \ln[4/(1-k^2)^{1/2}]$ as $k \to 1$.

Like solitons, cnoidal wave solutions—also referred to as Turing rolls when they are stable—develop a chirp when damping is present and do not have an exact analytical expression. However, the cnoidal wave solutions when the damping is

zero and $k \neq 1$ are characterized by an exponential falloff in the envelope of the comb spectrum that is more rapid than in the comb for the soliton solutions for which $k \to 1$, and we find that this exponential falloff is still present when the damping is nonzero. Due to this more rapid exponential falloff, these cnoidal wave solutions are not suitable for broadband comb generation, but are well-suited to narrowband comb applications, where limiting the number of comb lines and precisely controlling their amplitudes is desirable.

The outline of this paper is as follows: Section 2 presents the general Hamiltonian description of the lossless LLE equation for stationary (time-independent) solutions. Section 3 focuses on the derivation of the stationary cnoidal wave solutions in terms of Jacobi elliptic functions and elucidates the conditions under which the general family of solutions reduces to the soliton solution that has been described in [13]. Moreover, we discuss their periodicity, stability, and spectral properties. From an experimental perspective, it is also important to assess the spectral properties of the frequency combs generated by these cnoidal waves, as well as their accessibility from a broad range of initial conditions in the case of nonzero damping when analytical solutions are no longer available. Hence, in Section 4 we computationally study the periodic solutions in the presence of loss. We characterize their spectral properties, and we discuss their accessibility from impulsive initial conditions as a function of the external pump strength (h) and the damping or loss coefficient (α). We also discuss how these solutions apply to microresonators. Finally, in Section 5 we give our conclusions.

2. HAMILTONIAN APPROACH AND QUALITATIVE ANALYSIS

In this section, we qualitatively study the stationary solutions admitted by the LLE using a Hamiltonian approach. We categorize the different kinds of solutions and determine the parameter regime in which they are found. Following [13], we start with the master equation for the field evolution in microresonators:

$$\tau_0 \frac{\partial A}{\partial \tau} + \frac{i}{2}\beta_{2\Sigma}\frac{\partial^2 A}{\partial \xi^2} - i\gamma_\Sigma |A|^2 A = -\left(\alpha_\Sigma + \frac{T_c}{2} + i\delta_0\right)A + \sqrt{T_c}A_{\text{in}}, \tag{1}$$

where $A(\tau, \xi)$ is the slowly varying envelope of the electric field, τ is the slow time that parameterizes the evolution of the envelope, and ξ is the retarded time, also called fast time. We may write $\tau = z/V_g$, where z is the coordinate along the resonator circumference, V_g is the group velocity, and we may also write $\tau_0 = 2\pi R/V_g$, where τ_0 is the round-trip time and R is the radius of the resonator. We then find that $\omega_{\text{FSR}} = 2\pi/\tau_0$ is the free spectral range (FSR) in the resonator. If we denote the mode number of the dominant mode in the resonator as $\overline{m}$ and we denote the corresponding frequency as $\omega_{\overline{m}}$, we may write the normalized group velocity parameter $\beta_{2\Sigma} = (2\omega_{\overline{m}} - \omega_{\overline{m}+1} - \omega_{\overline{m}-1})\tau_0/\omega_{\text{FSR}}^2$. The parameter γ_Σ is the Kerr nonlinearity strength, α_Σ is the amplitude attenuation parameter per round trip, and $T_c/2$ is the coupling loss per round trip. If we let ω_p denote the frequency of the external pump, then we may define $\delta_0 = \tau_0(\omega_{\overline{m}} - \omega_p)$ as the normalized detuning of the frequency of the dominant mode from the frequency of the external pump. We also write the pump amplitude $A_{\text{in}} = \sqrt{P_0}\exp(i\phi_{\text{in}})$, where P_0 is the pump power, and ϕ_{in} is the pump phase. In this work, we consider the case of anomalous dispersion, i.e., $\beta_{2\Sigma} < 0$. Equation (1) can be recast in the form of a nondimensional LLE:

$$i\frac{\partial \psi}{\partial t} + \frac{\partial^2 \psi}{\partial x^2} - \psi + 2|\psi|^2\psi = -i\alpha\psi - h, \tag{2}$$

where $\psi = A[\gamma_\Sigma/(2\delta_0)]^{1/2}$ is the normalized complex envelope of the intracavity field, $t = \tau\delta_0/\tau_0$ is the normalized slow time, $x = \xi(2\delta_0/|\beta_{2\Sigma}|)^{1/2}$ is the normalized fast time, $\alpha = (\alpha_\Sigma + T_c/2)/\delta_0$ is the normalized damping or loss parameter, and $h = [T_c\gamma_\Sigma P_0/(2\delta_0^3)]^{1/2}[-i\exp(i\phi_{\text{in}})]$ is the normalized external pump amplitude, which is real and positive if we set $\phi_{\text{in}} = \pi/2$.

To obtain the stationary solutions of Eq. (2), we set the temporal derivative equal to zero, and obtain the equation

$$\frac{d^2\psi}{dx^2} + h + (i\alpha - 1)\psi + 2|\psi|^2\psi = 0. \tag{3}$$

This equation does not have analytical solutions that are expressible as Jacobi elliptic functions for $\alpha \neq 0$. Thus, our analytical discussion of solutions is focused on the lossless case. Without loss of generality, for $\alpha = 0$, the field ψ can be considered real, and Eq. (3) becomes

$$\frac{d^2\psi}{dx^2} + h - \psi + 2\psi^3 = 0. \tag{4}$$

Equation (4) has the Hamiltonian

$$H = \frac{1}{2}\left(\frac{d\psi}{dx}\right)^2 + V(\psi), \tag{5}$$

where V is the potential:

$$V = h\psi - \frac{\psi^2}{2} + \frac{\psi^4}{2}. \tag{6}$$

The Hamiltonian is constant at all x. Equation (5) can be integrated to yield the first-order differential equation:

$$\frac{d\psi}{dx} = \sqrt{2H - 2h\psi + \psi^2 - \psi^4}, \tag{7}$$

which can be solved by quadrature in terms of elliptic integrals [18]:

$$\int \mathrm{d}x = \int \frac{\mathrm{d}\psi}{\sqrt{2H - 2h\psi + \psi^2 - \psi^4}}. \tag{8}$$

The period of the solution is a function of h and H. In a microresonator, this period will be quantized, and we consider this issue explicitly in Section 4.

We observe that the potential in Eq. (6) is asymmetric with respect to ψ when the pump $h \neq 0$. As consequence, the cnoidal wave solutions will have a nonzero pedestal. This pedestal was already noted in the special case of solitons [13]. From Eq. (8), we obtain the equation

$$-\psi^4 + \psi^2 - 2h\psi + 2H = 0. \tag{9}$$

In the next section we will study the analytical solutions of Eq. (8); here, we provide a qualitative analysis that elucidates

the different regimes. The radicand of Eq. (8) is a quartic polynomial that has three extrema when $h < \sqrt{2/27}$, while it has only one extremum when $h > \sqrt{2/27}$. The discriminant of Eq. (9) is

$$\Delta = -2048H^3 - 512H^2 + 1152h^2H - 32H - 432h^4 + 16h^2. \tag{10}$$

We can rewrite Eq. (9) as

$$-(\psi - \psi_1)(\psi - \psi_2)(\psi - \psi_3)(\psi - \psi_4) = 0, \tag{11}$$

where the four roots $\psi_1, \psi_2, \psi_3, \psi_4$ of the quartic polynomial are, respectively,

$$\begin{aligned}
\psi_1 &= \frac{1}{2}\sqrt{t_3} + \frac{1}{2}\left(2 - t_3 - \frac{4h}{\sqrt{t_3}}\right)^{1/2},\\
\psi_2 &= \frac{1}{2}\sqrt{t_3} - \frac{1}{2}\left(2 - t_3 - \frac{4h}{\sqrt{t_3}}\right)^{1/2},\\
\psi_3 &= -\frac{1}{2}\sqrt{t_3} + \frac{1}{2}\left(2 - t_3 + \frac{4h}{\sqrt{t_3}}\right)^{1/2},\\
\psi_4 &= -\frac{1}{2}\sqrt{t_3} - \frac{1}{2}\left(2 - t_3 + \frac{4h}{\sqrt{t_3}}\right)^{1/2},
\end{aligned} \tag{12}$$

with

$$\begin{aligned}
t_1 &= -4(1-24H)^3 + (2-108h^2 + 144H)^2,\\
t_2 &= -2 + 108h^2 - 144H - \sqrt{t_1},\\
t_3 &= \frac{2}{3} + \frac{\sqrt[3]{2}(1-24H)}{3\sqrt[3]{t_2}} + \frac{\sqrt[3]{t_2}}{3\sqrt[3]{2}}.
\end{aligned} \tag{13}$$

Figures 1(a) and 1(b) show the potential V as a function of ψ for $h = 0.1$, so that $h < \sqrt{2/27}$, and for $h = 0.5$, so that $h > \sqrt{2/27}$. Their corresponding phase portraits are shown in Figs. 1(c) and 1(d), respectively. As shown in Fig. 1(a), for $h = 0.1$, the potential has three extrema, two of them are minima and one is a local maximum. The Hamiltonian at the local maximum corresponds to the soliton solutions of Eq. (4), which are represented by the separatrix of the phase space that is shown as line b in Fig. 1(c). The separatrix consists of two homoclinic orbits, which correspond to two different types of soliton solutions: the separatrix on the right corresponds to a positive soliton solution, and the separatrix on the left corresponds to a negative soliton solution with a positive pedestal. The positive and negative solitons are solutions of an externally driven damped nonlinear Schrödinger equation on an infinite line [19]. The periodic orbits, which are also called cycles, are related to the cnoidal wave solutions. Specifically, as we will discuss in Section 3, cycles outside the separatrix correspond to solutions that can be expressed in terms of the Jacobi elliptic cn functions, which we call cn-wave solutions. Cycles inside the separatrix can be expressed in terms of either dn or cn functions, and we call them dn-wave solutions. It is important to note that the soliton solutions are accessible when $h \le \sqrt{2/27}$, as shown in Fig. 1(c), while they are not accessible when $h > \sqrt{2/27}$, as shown Fig. 1(d).

We may separate the solutions of Eq. (4) into three cases:

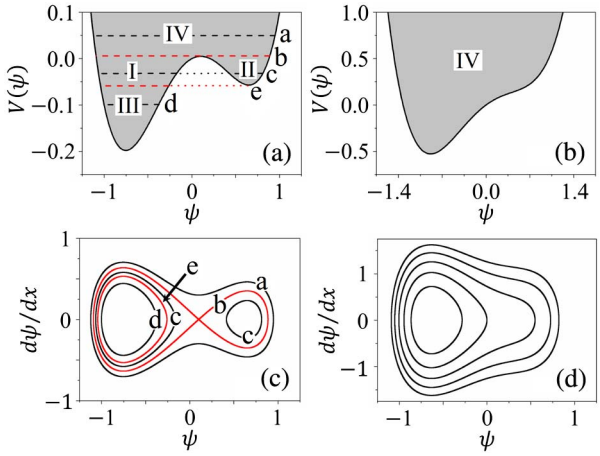

Fig. 1. Potential V and phase portraits of Eq. (4) for different magnitudes of the external pump h. The potential V is shown as a function of ψ, respectively, in (a) for $h = 0.1$ (three extrema) and in (b) for $h = 0.5$ (one extremum). The shaded areas are the regions where the solutions exist. Referring to (a), regions I and II are bounded by lines b and e, region III is below line e, and region IV is above line b. The lines a, b, c, and d correspond, respectively, to values of the Hamiltonian $H = 0.05$, $H = 0.00505$, $H = -0.03$, and $H = -0.1$. The radicand of Eq. (8) has four real solutions in regions I and II, while it has two real and two complex conjugate solutions in regions III and IV. The corresponding phase portraits are shown in the $(\psi, d\psi/dx)$-plane, respectively, in (c) for $h = 0.1$ and in (d) for $h = 0.5$.

(1) When $\Delta > 0$ and $\mathrm{Re}(2 - t_3 - 4h/\sqrt{t_3}) > 0$, the radicand of Eq. (8) has four real solutions, which corresponds to regions I and II in Fig. 1.

(2) When $\Delta < 0$, $\mathrm{Re}(2 - t_3 - 4h/\sqrt{t_3}) < 0$ and $\mathrm{Re}(2 - t_3 + 4h/\sqrt{t_3}) > 0$, the radicand of Eq. (8) has two real solutions and two complex conjugate solutions, which corresponds to region III in Fig. 1.

(3) When $\Delta < 0$ and $\mathrm{Re}(2 - t_3 - 4h/\sqrt{t_3}) > 0$, the radicand of Eq. (8) also has two real solutions and two complex conjugate solutions, which corresponds to region IV in Fig. 1.

In Section 3, we discuss the analytical solutions for these cases.

3. CNOIDAL WAVE SOLUTIONS WITH ZERO DAMPING ($\alpha = 0$)

In this section, we separately analyze the three cases that we have just identified, and we then show how the cnoidal wave solutions that are expressible in terms of Jacobi elliptic functions reduce to the soliton solutions that are expressible in terms of hyperbolic functions when the parameter k of the elliptic functions becomes equal to one. Finally, we analyze the periodicity, stability, and spectral properties of the cnoidal waves.

For each of the three cases, the solutions can be grouped into two sets: for $k = 1$, Set I reduces to the positive soliton solutions already found in [13], while Set II reduces to the negative soliton solutions of [13]. Figures 2 and 3 show, respectively, several examples of cnoidal wave solutions for Set I and Set II.

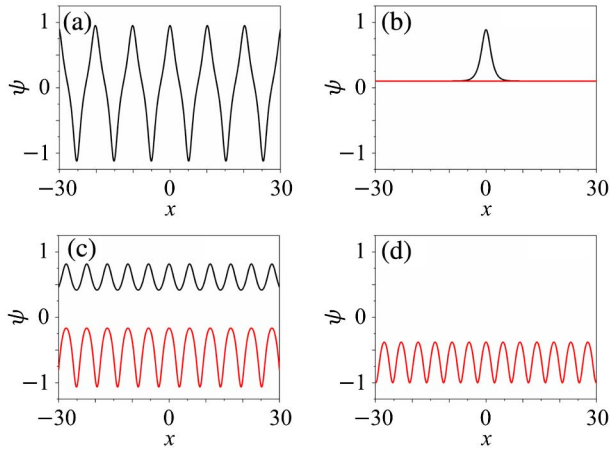

Fig. 2. Profiles of the cnoidal wave solutions ψ of Set I as a function of x with different values of Hamiltonian H for $h = 0.1$. The solutions in (a)–(d) correspond to the lines a, b, c, and d in Figs. 1(a) and 1(c), respectively. Line b is the separatrix where soliton solutions are found. (a) We show the cnoidal wave solution at $H = 0.05$. (b) We show the two possible solutions at $H = 0.00505$, the positive soliton solution (black curve) and the continuous-wave solution (red curve). (c) We show the cnoidal wave solutions with $H = -0.03$. The upper curve (positive cnoidal wave) is the solution corresponding to the closed orbit c located at $\psi > 0$ in Fig. 1(c). The lower curve (negative cnoidal wave) is the solution corresponding to the closed orbit c located at $\psi < 0$ in Fig. 1(c). (d) We show the cnoidal wave solution with $H = -0.1$ corresponding to the closed orbit d.

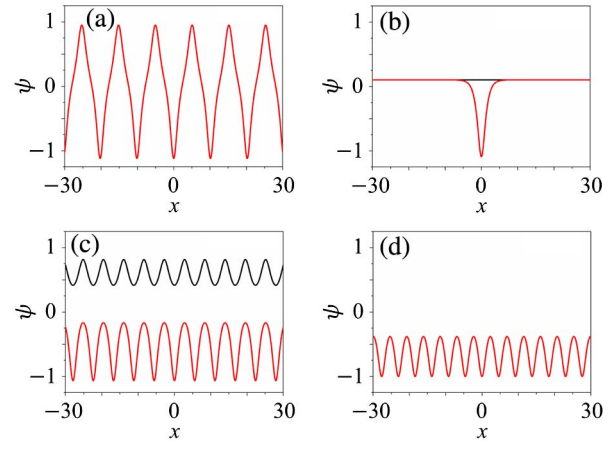

Fig. 3. Solutions ψ of Set II as a function of x at different values of the Hamiltonian H for $h = 0.1$. The solutions in (a)–(d) correspond to the lines a, b, c, and d in Figs. 1(a) and 1(c), respectively. We show (a) the cnoidal wave solution at $H = 0.05$, (b) the negative soliton solution and the continuous-wave solution at $H = 0.00505$, (c) the positive and negative cnoidal wave solutions at $H = -0.03$, and (d) the cnoidal wave solution at $H = -0.1$.

A. Cnoidal Wave Solutions of Set I

1. $\Delta > 0$ *and* $\mathrm{Re}(2 - t_3 - 4h/\sqrt{t_3}) > 0$

When $\Delta > 0$ and $\mathrm{Re}(2 - t_3 - 4h/\sqrt{t_3}) > 0$, the radicand of Eq. (8) has four real roots.

For $\psi_4 \le \psi < \psi_3$, we have

$$\psi = \psi_{+\mathrm{dn1}} = \frac{F\psi_3 - C\psi_2}{F - C} \times \left[1 + \frac{\frac{2FC(\psi_2-\psi_3)}{(F\psi_3-C\psi_2)(F+C)}}{1 + \frac{F-C}{F+C}\,\mathrm{nd}\left(\frac{x}{g_{\mathrm{nd}}}\middle|k_{\mathrm{nd}}^2\right)}\right], \tag{14}$$

and for $\psi_2 \le \psi < \psi_1$, we have

$$\psi = \psi_{+\mathrm{dn2}} = \frac{F\psi_1 + B\psi_4}{F + B} \times \left[1 + \frac{\frac{2FB(\psi_1-\psi_4)}{(F\psi_1+B\psi_4)(F-B)}}{1 + \frac{F+B}{F-B}\,\mathrm{nd}\left(\frac{x}{g_{\mathrm{nd}}}\middle|k_{\mathrm{nd}}^2\right)}\right], \tag{15}$$

where $\mathrm{nd}(x|k^2) = 1/\mathrm{dn}(x|k^2)$ is the inverse of $\mathrm{dn}(x|k^2)$ [18]:

$$\begin{aligned} B &= \psi_1 - \psi_2 = \left(2 - t_3 - 4h/\sqrt{t_3}\right)^{1/2}, \\ C &= \psi_3 - \psi_4 = \left(2 - t_3 + 4h/\sqrt{t_3}\right)^{1/2}, \\ F &= (\psi_2 - \psi_4)k_d, \\ g_{\mathrm{nd}} &= g_d/(1 + k_d), \\ k_{\mathrm{nd}} &= 2\sqrt{k_d/(1 + k_d)}, \end{aligned} \tag{16}$$

with

$$g_d = 2/\sqrt{(\psi_1 - \psi_3)(\psi_2 - \psi_4)}, \tag{17}$$

and

$$k_d = \left[\frac{(\psi_1 - \psi_2)(\psi_3 - \psi_4)}{(\psi_1 - \psi_3)(\psi_2 - \psi_4)}\right]^{1/2}. \tag{18}$$

The profiles of the cnoidal wave solutions for $H = 0$ and $h = 0.1$ are shown in Fig. 2(c).

2. $\Delta < 0$, $\mathrm{Re}(2 - t_3 - 4h/\sqrt{t_3}) < 0$, *and* $\mathrm{Re}(2 - t_3 + 4h/\sqrt{t_3}) > 0$

When $\Delta < 0$, $\mathrm{Re}(2 - t_3 - 4h/\sqrt{t_3}) < 0$, and $\mathrm{Re}(2 - t_3 + 4h/\sqrt{t_3}) > 0$, the radicand of Eq. (8) has two real roots and a pair of complex conjugate roots. Here, the real roots are ψ_3 and ψ_4, while the complex conjugate roots are ψ_1 and ψ_2. We let $\psi_1 = \rho_{c1} + i\eta_{c1}$ and $\psi_2 = \rho_{c1} - i\eta_{c1}$.

For $\psi_4 \le \psi < \psi_3$, we have

$$\psi = \psi_{+\mathrm{cn3}} = \frac{B_{c1}\psi_3 + A_{c1}\psi_4}{B_{c1} + A_{c1}} \times \left[1 + \frac{\frac{2A_{c1}B_{c1}(\psi_3-\psi_4)}{(B_{c1}\psi_3+A_{c1}\psi_4)(B_{c1}-A_{c1})}}{1 + \frac{B_{c1}+A_{c1}}{B_{c1}-A_{c1}}\,\mathrm{nc}\left(\sqrt{A_{c1}B_{c1}}x\middle|k_3^2\right)}\right], \tag{19}$$

where $\mathrm{nc}(x|k^2) = 1/\mathrm{cn}(x|k^2)$ is the inverse of the Jacobian elliptic cosine function $\mathrm{cn}(x|k^2)$ [18]:

$$\begin{aligned} A_{c1} &= [(\rho_{c1} - \psi_3)^2 + \eta_{c1}^2]^{1/2}, \\ B_{c1} &= [(\rho_{c1} - \psi_4)^2 + \eta_{c1}^2]^{1/2}, \\ k_3 &= \left[\frac{(\psi_3 - \psi_4)^2 - (A_{c1} - B_{c1})^2}{4A_{c1}B_{c1}}\right]^{1/2}. \end{aligned} \tag{20}$$

The profile of the cnoidal wave solution for $H = -0.1$ and $h = 0.1$ is shown in Fig. 2(d).

3. $\Delta < 0$ *and* $\mathrm{Re}(2 - t_3 - 4h/\sqrt{t_3}) > 0$

When $\Delta < 0$ and $\mathrm{Re}(2 - t_3 - 4h/\sqrt{t_3}) > 0$, the radicand of Eq. (8) also has two real roots and a pair of complex conjugate

roots. Here, the real roots are ψ_1 and ψ_4, while the complex conjugate roots are ψ_2 and ψ_3. We let $\psi_2 = \rho_{c2} + i\eta_{c2}$ and $\psi_3 = \rho_{c2} - i\eta_{c2}$.

For $\psi_4 \le \psi < \psi_1$, we have

$$\psi = \psi_{+\mathrm{cn}4} = \frac{B_{c2}\psi_1 + A_{c2}\psi_4}{B_{c2} + A_{c2}} \times \left[1 + \frac{\frac{2A_{c2}B_{c2}(\psi_1-\psi_4)}{(B_{c2}\psi_1+A_{c2}\psi_4)(B_{c2}-A_{c2})}}{1 + \frac{B_{c2}+A_{c2}}{B_{c2}-A_{c2}}\mathrm{nc}\left(\sqrt{A_{c2}B_{c2}}x\middle|k_4^2\right)}\right], \tag{21}$$

where

$$\begin{aligned} A_{c2} &= [(\rho_{c2} - \psi_1)^2 + \eta_{c2}^2]^{1/2}, \\ B_{c2} &= [(\rho_{c2} - \psi_4)^2 + \eta_{c2}^2]^{1/2}, \\ k_4 &= \left[\frac{(\psi_1 - \psi_4)^2 - (A_{c2} - B_{c2})^2}{4A_{c2}B_{c2}}\right]^{1/2}. \end{aligned} \tag{22}$$

We show the profile of the cnoidal wave solution for $H = 0.01$ and $h = 0.1$ in Fig. 2(a).

B. Cnoidal Wave Solutions of Set II

1. $\Delta > 0$ *and* $\mathrm{Re}(2 - t_3 - 4h/\sqrt{t_3}) > 0$

When $\Delta > 0$ and $\mathrm{Re}(2 - t_3 - 4h/\sqrt{t_3}) > 0$, the radicand of Eq. (8) has four real roots.

For $\psi_4 < \psi \le \psi_3$, we have

$$\psi = \psi_{-\mathrm{dn}1} = \frac{C\psi_1 + E\psi_4}{C + E} \times \left[1 + \frac{\frac{2\,CE(\psi_1-\psi_4)}{(C\psi_1+E\psi_4)(C-E)}}{1 - \frac{C+E}{C-E}\mathrm{nd}\left(\frac{x}{g_{\mathrm{nd}}}\middle|k_{\mathrm{nd}}^2\right)}\right], \tag{23}$$

and for $\psi_2 < \psi \le \psi_1$, we have

$$\psi = \psi_{-\mathrm{dn}2} = \frac{B\psi_3 - E\psi_2}{B - E} \times \left[1 + \frac{\frac{2BE(\psi_2-\psi_3)}{(B\psi_3-E\psi_2)(B+E)}}{1 - \frac{B-E}{B+E}\mathrm{nd}\left(\frac{x}{g_{\mathrm{nd}}}\middle|k_{\mathrm{nd}}^2\right)}\right], \tag{24}$$

where $E = (\psi_1 - \psi_3)k_d$, B, C, g_{nd}, k_{nd} are defined in Eq. (14). The profile of the cnoidal wave solutions for $H = 0$ and $h = 0.1$ is shown in Fig. 3(c).

2. $\Delta < 0$, $\mathrm{Re}(2 - t_3 - 4h/\sqrt{t_3}) < 0$, *and* $\mathrm{Re}(2 - t_3 + 4h/\sqrt{t_3}) > 0$

When $\Delta < 0$, $\mathrm{Re}(2 - t_3 - 4h/\sqrt{t_3}) < 0$, and $\mathrm{Re}(2 - t_3 + 4h/\sqrt{t_3}) > 0$, the radicand of Eq. (8) has two real roots and a pair of complex conjugate roots. Here, the real roots are ψ_3 and ψ_4, while the complex conjugate roots are ψ_1 and ψ_2. We let $\psi_1 = \rho_{c1} + i\eta_{c1}$ and $\psi_2 = \rho_{c1} - i\eta_{c1}$.

For $\psi_4 < \psi \le \psi_3$, we have

$$\psi = \psi_{-\mathrm{cn}3} = \frac{B_{c1}\psi_3 + A_{c1}\psi_4}{B_{c1} + A_{c1}} \times \left[1 + \frac{\frac{2A_{c1}B_{c1}(\psi_3-\psi_4)}{(B_{c1}\psi_3+A_{c1}\psi_4)(B_{c1}-A_{c1})}}{1 - \frac{B_{c1}+A_{c1}}{B_{c1}-A_{c1}}\mathrm{nc}\left(\sqrt{A_{c1}B_{c1}}x\middle|k_3^2\right)}\right], \tag{25}$$

where A_{c1}, B_{c1}, and k_3 are defined in Eq. (19). The profile of the cnoidal wave solution for $H = -0.1$ and $h = 0.1$ is shown in Fig. 3(d).

3. $\Delta < 0$ *and* $\mathrm{Re}(2 - t_3 - 4h/\sqrt{t_3}) > 0$

When $\Delta < 0$ and $\mathrm{Re}(2 - t_3 - 4h/\sqrt{t_3}) > 0$, the radicand of Eq. (8) also has two real roots and a pair of complex conjugate roots. Here the real roots are ψ_1 and ψ_4, while the complex conjugate roots are ψ_2 and ψ_3. We let $\psi_2 = \rho_{c2} + i\eta_{c2}$ and $\psi_3 = \rho_{c2} - i\eta_{c2}$.

For $\psi_4 < \psi \le \psi_1$, we have

$$\psi = \psi_{-\mathrm{cn}4} = \frac{B_{c2}\psi_1 + A_{c2}\psi_4}{B_{c2} + A_{c2}} \times \left[1 + \frac{\frac{2A_{c2}B_{c2}(\psi_1-\psi_4)}{(A_{c2}\psi_4+B_{c2}\psi_1)(B_{c2}-A_{c2})}}{1 - \frac{B_{c2}+A_{c2}}{B_{c2}-A_{c2}}\mathrm{nc}\left(\sqrt{A_{c2}B_{c2}}x\middle|k_4^2\right)}\right], \tag{26}$$

where A_{c2}, B_{c2}, and k_4 are defined in Eq. (21). The profile of the cnoidal wave solution for $H = 0.01$ and $h = 0.1$ is shown in Fig. 3(a).

C. Limiting Case of the Lossless Soliton Solutions

The cnoidal waves that are expressible in terms of Jacobi elliptic functions reduce to soliton solutions that are expressible in terms of hyperbolic functions when the parameter k of the elliptic functions $\mathrm{cn}(x|k^2)$ and $\mathrm{dn}(x|k^2)$ becomes equal to 1.

We first write the positive and negative soliton solutions of the LLE as [13]

$$\psi_\pm = \psi_0\left[1 + \frac{M_1}{1 \pm M_2\,\cosh(M_3 x)}\right], \tag{27}$$

where

$$\begin{aligned} M_1 &= 2(X - 1), \\ M_2 &= \sqrt{X}, \\ M_3 &= \sqrt{2(X - 1)/(2X + 1)}, \\ \psi_0 &= 1/\sqrt{2(1 + 2X)}, \end{aligned} \tag{28}$$

and X is the solution of the equation

$$\sqrt{2}X/(1 + 2X)^{3/2} = h. \tag{29}$$

We find that our Eqs. (15) and (21) reduce to the positive soliton solution of Eq. (27), as shown in Fig. 2(b), while Eqs. (23) and (26) reduce to the negative soliton solution of Eq. (27) as shown in Fig. 3(b).

D. Periodicity, Stability, and Spectral Properties of the Lossless Cnoidal Wave Solutions

Figure 4 shows the period P in the (h, H) plane. For a fixed value of h, the period P of different cnoidal waves will be different. As a consequence, the spacing of the comb lines in their Fourier spectrum is different. In particular, as k approaches 1 and the solutions approach soliton solutions, the period P tends to infinity, and the comb lines become more closely spaced. Moreover, only stable cnoidal waves can generate reliable frequency combs. Thus, it is important to study both the periodicity and the stability of the cnoidal wave solutions. The computational study of the stability of cnoidal waves has been performed by the numerical integration of Eq. (2) in the time domain with $\alpha = 0$ using a split-step algorithm [20] in which the initial conditions are the stationary cnoidal wave solutions of Eq. (4) that we have just derived. We show the results in

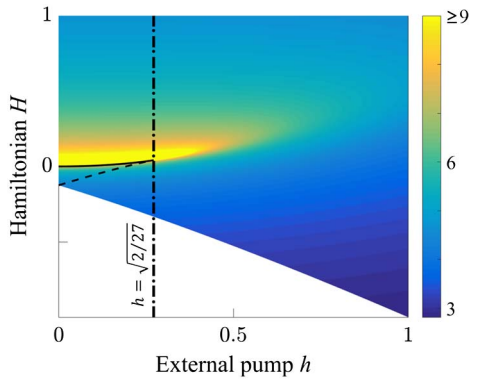

Fig. 4. Period of the cnoidal waves in the (h, H) plane. The solid line indicates the loci of points in the parameter space where soliton solutions exist for which $P \to +\infty$. The region bounded by the solid line and by the dashed line is where positive and negative cnoidal wave/soliton solutions coexist. The vertical dashed–dotted line indicates the value of the pump at $h = \sqrt{2/27}$.

Fig. 5. The small numerical noise intrinsic to the numerical method that we use to calculate the temporal evolution acts as a perturbation on the analytical solution. Hence, we expect

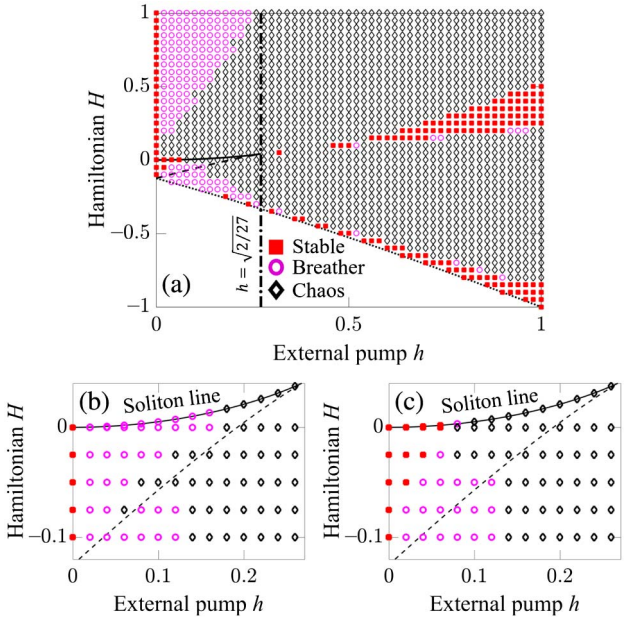

Fig. 5. (a) Results of a computational study to assess the stability of the cnoidal waves in the (h, H) plane. The solid line indicates the loci of points in the parameter space where soliton solutions exist. The region bounded by the solid line and by the dashed line is where positive and negative cnoidal wave/soliton solutions coexist. Here we report the results of the stability study for the negative solutions. The dotted line indicates the boundary of the existence region of cnoidal wave solutions, and the vertical dashed–dotted line indicates the value of the pump at $h = \sqrt{2/27}$. (b) Magnification of the region where positive and negative solution coexist. Here we report the results of the stability study for the positive solutions. The solutions are always unstable for $h \neq 0$. (c) The solutions are the same as in (b) except that here we report the results for the negative solutions. In this case, stable negative soliton solutions and stable cnoidal waves exist.

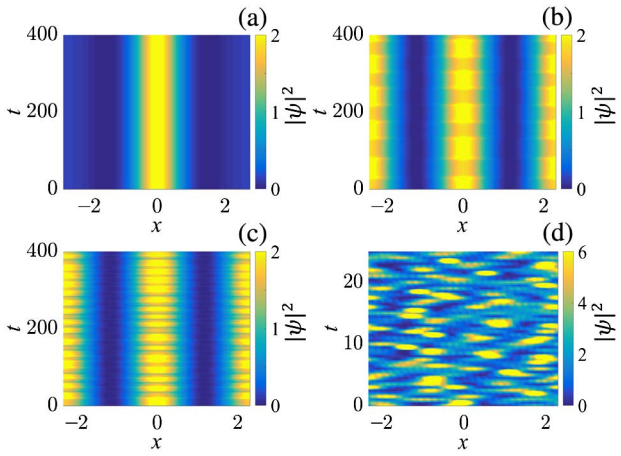

Fig. 6. Spatiotemporal evolution of the intensity of the cnoidal wave for different values of H and h. The x-coordinate runs over one period of the cnoidal wave. The figure exemplifies four typical cases. (a) The cnoidal wave remains stable for $h = 0.7$ and $H = 0.2$. (b) The cnoidal wave evolves to a breather for $h = 0.16$ and $H = 1$. (c) The cnoidal wave generates temporal chaos for $h = 0.26$ and $H = 1$. (d) The cnoidal wave generates spatiotemporal chaos for $h = 0.45$ and $H = 1$.

that the profile of the analytical solution remains nearly unchanged during its temporal evolution if the solution is stable; otherwise we expect that the solution diverges from the stationary solution. In this case, we find computationally that the solution undergoes periodic oscillations or becomes chaotic. This

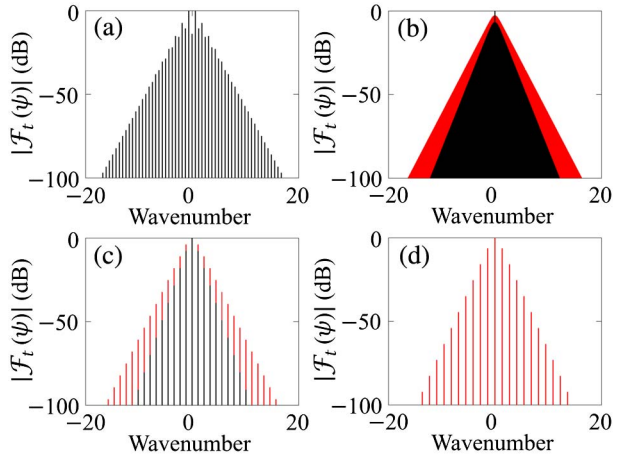

Fig. 7. Absolute value of the Fourier transform $(\mathcal{F}_t)$ of the cnoidal wave solutions that are plotted in Figs. 2 and 3, respectively. The wavenumber equals $(m - \bar{m})2\pi/P$, where $\bar{m}$ is the mode number of the dominant mode. (a) Fourier spectra of the cnoidal waves that are plotted in Figs. 2(a) and 3(a) with $H = 0.05$. The Fourier spectra are the same because the solutions in Figs. 2(a) and 3(a) are the same except for a constant shift. (b) Fourier spectra of the positive soliton solution (narrower spectrum) that are plotted in Fig. 2(b) and of the negative soliton solution (wider spectrum) that are plotted in Fig. 3(b) with $H = -0.00505$. (c) Fourier spectra of the positive and negative cnoidal waves that are plotted in Figs. 2(c) and 3(c) with $H = -0.03$. The Fourier spectra of the positive and negative solutions of Figs. 2(c) and 3(c) are the same. (d) Fourier spectra of the cnoidal waves that are plotted in Figs. 2(d) and 3(d) with $H = -0.1$.

approach produces ambiguous results near the stability boundary, as is apparent in Fig. 5. Linearization of the evolution equations, combined with a spectral analysis of the linearized equations, would have to be used to unambiguously determine the boundary. However, the ambiguous region is narrow in this case and does not affect our conclusions. So, we did not carry out this more refined study. Three regions of stability for the cnoidal waves in the (h, H) plane are present. The first one lies at the border of the domain of the allowed solutions, close to where the Hamiltonian H intersects the potential V at its absolute minimum. These solutions might not be interesting from an experimental perspective because of their small amplitude. A second region of stability is visible in Fig. 5(c). The stable solutions lie in the region bounded by the soliton line, the dashed–dotted line, and the $h = 0$ axis. These cnoidal wave solutions are akin to the stable negative soliton solutions studied in the past for the ac-driven, nonlinear Schrödinger equation on an infinite line [19]. However, we note that the stability region is confined to small values of the external pump h with $h \lesssim 0.05$. Hence, small fluctuations of the average power of the external pump might destabilize the system, turning the stable solutions into breathers or chaotic states.

Yet a third region of stability is visible in Fig. 5(a). In this case, the stable solutions are obtained for $h \gtrsim 0.5$, $H \gtrsim 0$, and periodicity $4 \lesssim P \lesssim 6$. These solutions should be visible in experiments, especially in practical situations where loss in the microresonator is important and, thus, higher pump power would be needed to generate a comb. A study of the accessibility of these stable solutions in the practical case where losses are considered will be presented in the next section. An example of the evolution of the cnoidal waves for different values of H and h is provided in Fig. 6.

It may seem surprising at first that it is possible to obtain stable solutions when $\alpha = 0$ since the pump is nonzero. However, an analysis of Eq. (2) shows that the pump adds no energy to the solution when $\int_{-P/2}^{P/2} h(\psi - \psi^*)\mathrm{d}x = 0$, which is the case for all the analytical solutions. Physically, this condition implies that the pump is out of phase with

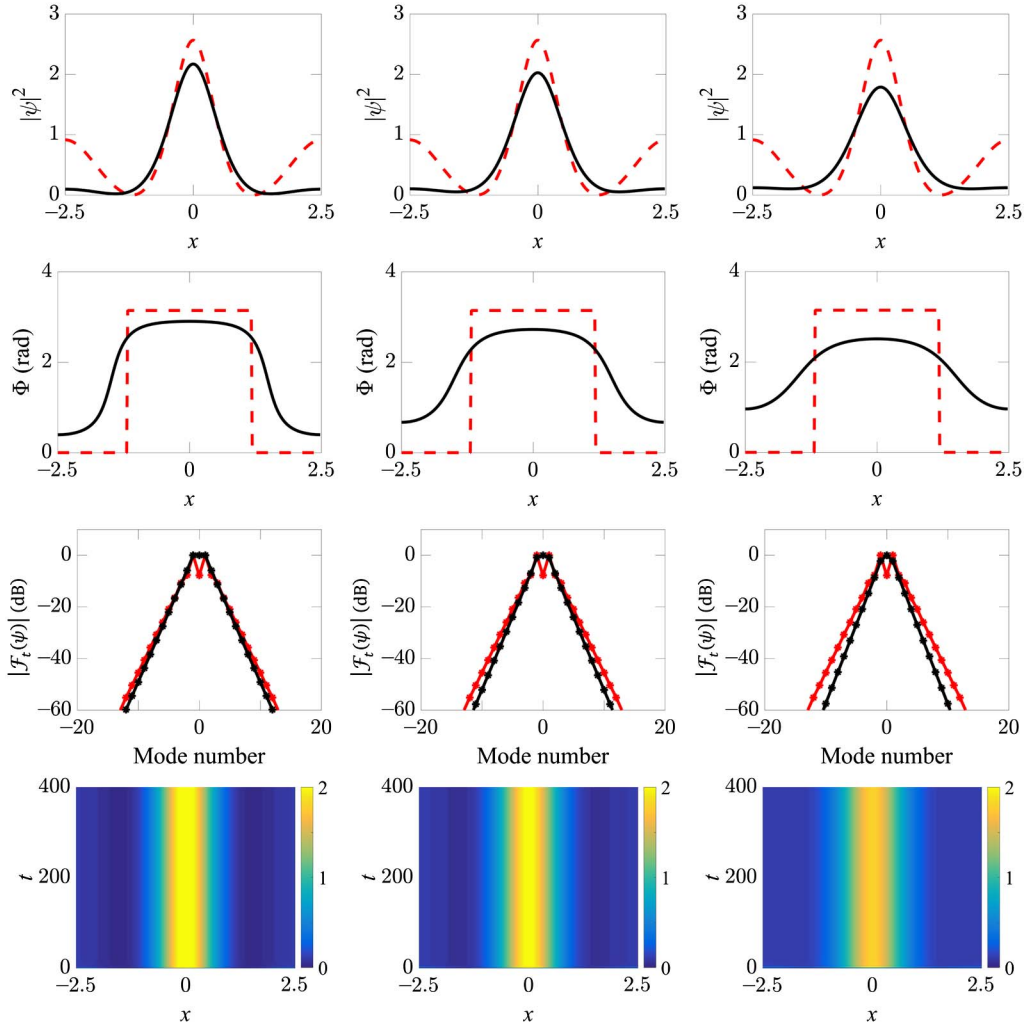

Fig. 8. First row: the stationary analytical solutions (dashed line) calculated for $H = 0.72$ and $h = 0.8$ ($P = 5$) and used as initial conditions for the numerical integration are compared to the computational solutions (continuous line) at $t = 400$ for $\alpha = 0.3$, 0.5, and 0.7, respectively. At this time, the solution has converged to its stationary value. Second row: the phases of the analytical and computational solutions are compared. Third row: Fourier spectra of the analytical and computational solutions. Fourth row: spatiotemporal evolution of the numerical solutions.

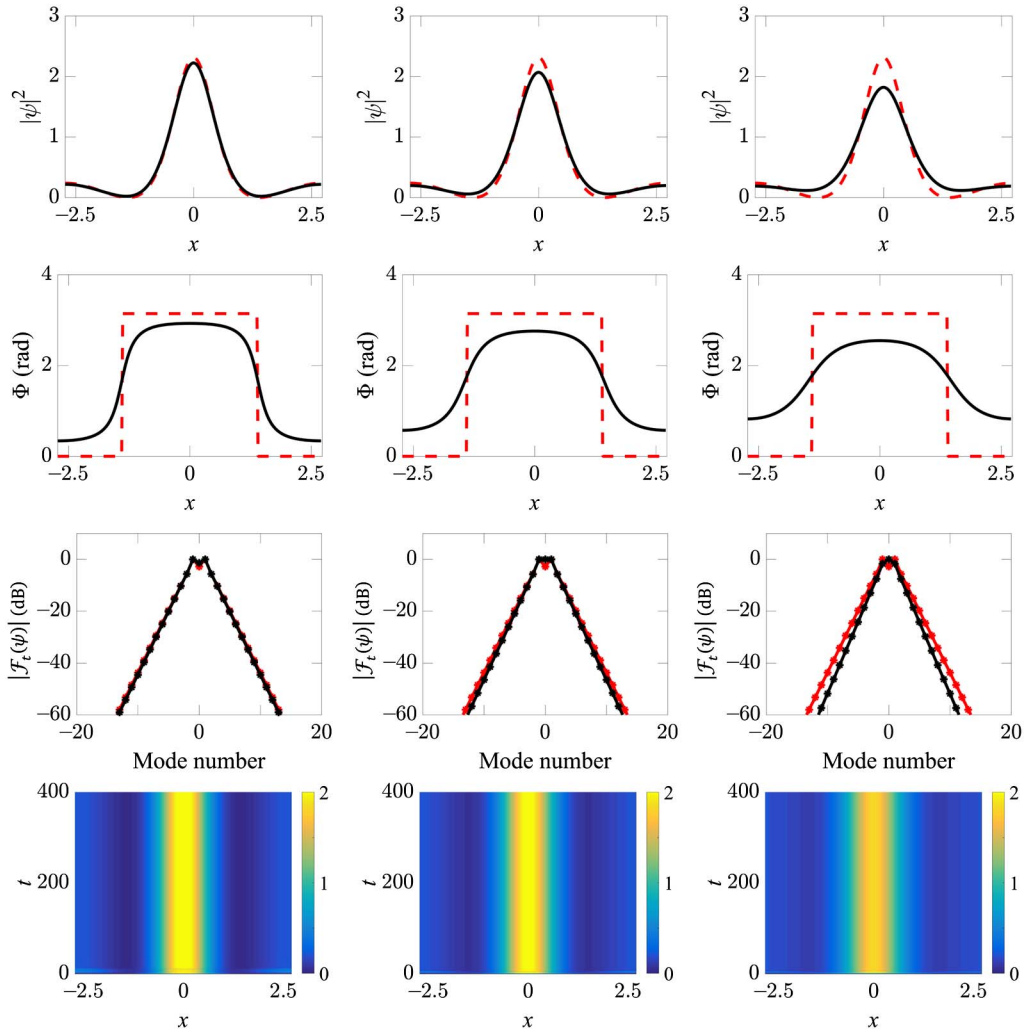

Fig. 9. Same as in Fig. 8 except that here $h = 0.8$ and $H = 0.3$ ($P = 5.4$).

the cnoidal waves. We have found that even when the solutions are unstable, they are chaotic or oscillatory and do not blow up.

In Fig. 7, we show the Fourier spectra of the cnoidal waves and of the positive and negative solitons for the solutions reported in Figs. 2 and 3. It is seen that the Fourier spectra all have a triangular shape on a logarithmic scale, indicating an exponential falloff. This triangular shape is a typical signature of the spectrum of parametrically driven systems where the energy is transferred from the dominant spectral component to the sideband spectral components due to the modulational instability induced by four-wave mixing [21]. We see that all the spectra look similar, except for the spacing of the spectral lines. As the period grows, the spacing of the spectral lines diminishes. In principle, for the soliton solution at $k = 1$ for which $P \to \infty$, the spacing becomes zero and there are no longer individual spectral lines.

In a microresonator, the spacing between the comb lines is fixed by the device, and the spacing of the spectral lines must be a multiple M of the device's FSR. The soliton solutions in microresonators correspond to k-values that are slightly less

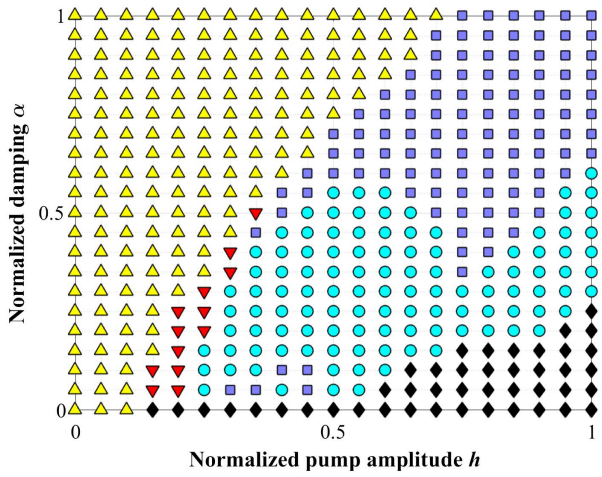

Fig. 10. Accessibility chart for period $P = 5$ in the (h, α) plane. Purple squares are stable cnoidal waves; yellow upward triangles are cw waves; red downward triangles are bistable solutions; cyan circles are breathers; black diamonds are chaos.

than 1. By appropriately choosing the device parameters and pump strength when the cnoidal waves exist stably and are accessible, it is possible to choose a desirable k-value and multiple M of the FSR and thereby tailor a comb with a desired spectral spacing and exponential falloff. In particular, we note that cnoidal waves in regions II, III, and IV that are near the bottom of the potential well will have nearly sinusoidal oscillations and a rapid spectral falloff. Generating cnoidal waves with M periods in the microresonator will lead to a spectral spacing that is M times the FSR. Widely spaced comb lines with a rapid exponential falloff would be useful, for example, in the search for earth-like planets [10].

4. CNOIDAL WAVES IN THE CASE OF NONZERO DAMPING ($\alpha \neq 0$)

When $\alpha \neq 0$, we no longer find stationary solutions analytically. Instead, we find them, when they are stable, by numerically integrating Eq. (2) with a split-step algorithm [20] using the analytical solutions of Eq. (4) as the initial conditions. We find that the stationary solutions are no longer real functions, as was the case with zero damping. They are complex functions $\psi(x) = |\psi(x)| \exp[i\Phi(x)]$ with a periodic phase modulation $\Phi(x)$. Figures 8 and 9 show a comparison between the stationary analytical solutions calculated for $\alpha = 0$ and the numerical solutions calculated by integration of Eq. (2) for $\alpha = 0.3$, 0.5, and 0.7 and for the initial conditions that are given by the analytical solutions of Eq. (4) with the following parameters: $h = 0.8$ and $H = 0.72$ ($P = 5$) for Fig. 8, and $h = 0.8$ and $H = 0.3$ ($P = 5.4$) for Fig. 9. In both figures, it is apparent that the stationary analytical solution used as the initial condition rapidly evolves into a stable stationary solution. While it is not a solution that can be expressed analytically in terms of Jacobi elliptic functions, the period, shape, and spectral properties remain closely to those of the analytical solutions that are used as the initial conditions. We also note that the stationary analytical solution used in Fig. 8 is unstable as shown in Fig. 5, while the numerical calculation shows that the final state that is reached with loss is stable. The introduction of loss enlarges the parameter range in which the cnoidal waves are stable. This behavior is expected because the loss acts as a filter that damps the high wave vector components of the field, thereby improving the solution's stability. The damping of the high wave vector components can be seen in Figs. 8 and 9 by comparing the narrower Fourier spectra of the computational solutions with the slightly broader Fourier spectra of the analytical solutions. To demonstrate that these cnoidal wave solutions are accessible from a broader set of initial conditions than the analytical cnoidal wave solutions at $\alpha = 0$, we have solved Eq. (2) numerically using two impulsive functions as the initial conditions. The first impulsive function is 10^5 at $x = 0$ and 0 everywhere else. The second impulsive function is 10^{-5} at $x = 0$ and 0 everywhere else. In Fig. 10 we show an accessibility chart in the (h, α) plane for $P = 5$. If both initial conditions lead to unstable chaotic behavior, we plot a diamond. If both initial conditions lead to breathers that are periodic in t as well as in x, we plot a dot. If both solutions are plane waves, we plot a triangle. If the larger impulsive function leads to a breather and the smaller impulsive function leads to a plane wave, we plot an inverted triangle. Finally, if both initial conditions lead to a cnoidal wave, we plot a square. We see that there is a broad range of parameters from which the cnoidal waves are accessible from impulsive initial conditions. We also note that the parameter range in which stable cnoidal waves exist is significantly larger, but, as α decreases, the stable solutions no longer can be accessed from impulsive initial conditions. In Fig. 11, we show four typical examples of the spatiotemporal evolution of the field intensity with the low amplitude impulsive function as the initial condition. A systematic study of the accessibility of cnoidal waves with nonzero damping will be the subject of future investigations.

We now present an example to show how the nondimensional parameters are related to the physical parameters of a microresonator. We consider a microresonator made of magnesium fluoride (MgF_2) with radius $R = 0.1$ cm, and with linear and nonlinear refractive indices $n_0 = 1.38$ and $n_2 = 0.9 \times 10^{-16}$ cm^2/W at the wavelength $\lambda_0 = 1.5$ μm [13]. The group velocity dispersion parameter is $\beta_{2\Sigma} = -2.8 \times 10^{-5}$ ps^2. For a mode volume $V = 2 \times 10^{-7}$ cm^3, we obtain the Kerr nonlinearity strength $\gamma_\Sigma = (2\pi R)^2 n_2 \omega_0/(cV) = 7.9 \times 10^{-6}$ W^{-1}. The round-trip time τ_0 can be approximately calculated as $\tau_0 \simeq 2\pi R n_0/c$, which implies for the current choice of parameters $\tau_0 \simeq 29$ ps. For a detuning $(\omega_{\overline{m}} - \omega_p) \simeq 2$ MHz, the normalized detuning is $\delta_0 = \tau_0(\omega_{\overline{m}} - \omega_p) \simeq 5.8 \times 10^{-5}$. For a coupling parameter $T_c \simeq 4 \times 10^{-5}$ and an amplitude loss per round trip $a_\Sigma \simeq 2 \times 10^{-5}$, the normalized loss parameter is $\alpha = (\alpha_\Sigma + T_c/2)/\delta_0 \simeq 0.7$. For these values, we find that the fast time ξ in picoseconds is related to the normalized fast time x as $\xi(\text{ps}) \simeq 0.5x$, the slow time τ in microseconds is related to the normalized slow time t as $\tau(\mu\text{s}) \simeq 0.5t$, and the external pump power P_0 in milliwatts is related to the normalized field amplitude h as $P_0(\text{mW}) \simeq 100h^2$. The

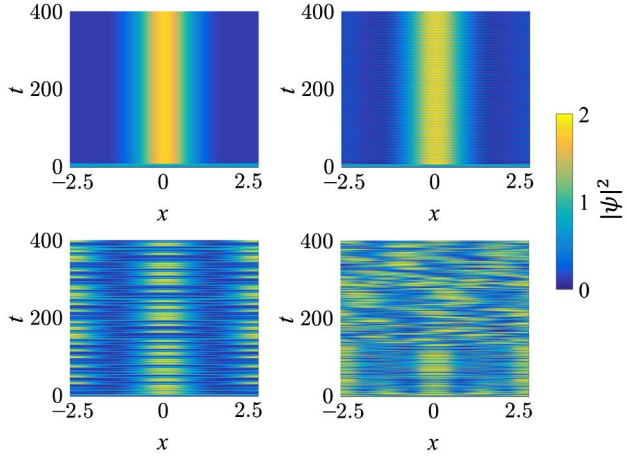

Fig. 11. Spatiotemporal evolution of the field intensity for different values of α and h corresponding to the points contained in the accessibility chart of Fig. 10. In this case, the initial condition is the small amplitude (10^{-5}) impulsive function. We show four typical cases. (a) The impulsive function evolves to a stable cnoidal wave for $\alpha = 0.7$ and $h = 0.8$. (b) The impulsive function evolves to a breather for $\alpha = 0.4$ and $h = 0.6$. (c) The impulsive function generates temporal chaos for $\alpha = 0.25$ and $h = 0.45$. (d) The impulsive function generates spatiotemporal chaos for $\alpha = 0.05$ and $h = 0.75$.

cnoidal wave described in the third column of Fig. 9 ($P = 5.4$, $h = 0.8$, $\alpha = 0.7$) will have a period of 2.7 ps and, hence, we expect 10 or 11 periods will appear in the resonator round-trip time of 29 ps for a pump level of approximately 60 mW. With 10 periods in the resonator, the comb lines are spaced 340 GHz apart. The amplitudes of the lines at $m = \bar{m} \pm 1$ are down from the peak line at $m = \bar{m}$ by 2 dB, and the amplitudes of the lines at $m = \bar{m} \pm 2$ are down from the peak by 10 dB.

5. CONCLUSIONS

In conclusion, we have studied both analytically and computationally the family of cnoidal wave solutions to the LLE. We have shown computationally that these cnoidal waves can be stable and are accessible from a wide range of values of the external pump and of the damping. Hence, these cnoidal waves can be used for nonlinear frequency comb generation in cases in which solitons are difficult to generate and/or the microresonator losses are substantial and, hence, higher external power are necessary to sustain the comb generation. Moreover, their inherently coarse-tooth characteristic will be useful when limiting the number of comb lines and precisely controlling their amplitudes is required, as, for example, in the precise generation of new frequencies [8], quantum networking [9], or astrocombs [10]. In future work, we will investigate in greater detail the accessibility and stability of cnoidal wave solutions when loss is included. The approach used in this paper can also be applied to Kerr comb generation in the normal dispersion regime, which should also be the subject of future work.

Funding. Aviation and Missile Research, Development, and Engineering Center (AMRDEC)/Defense Advanced Research Projects Agency (DARPA) (W31P4Q-14-1-0002); Army Research Laboratory (ARL) (W911NF-13-2-0010).

Acknowledgment. The simulations were carried out at UMBC's high performance computing facility. We thank Shaokang Wang for helpful discussions.

REFERENCES

1. J. D. Jost, T. Herr, C. Lecaplain, V. Brasch, M. H. P. Pfeiffer, and T. J. Kippenberg, "Counting the cycles of light using a self-referenced optical microresonator," Optica **2**, 706–711 (2015).
2. P. Del'Haye, A. Coillet, T. Fortier, K. Beha, D. C. Cole, K. Y. Yang, H. Lee, K. J. Vahala, S. B. Papp, and S. A. Diddams, "Phase-coherent microwave-to-optical link with a self-referenced microcomb," Nat. Photonics **10**, 516–520 (2016).
3. P. Del'Haye, A. Schliesser, O. Arcizet, T. Wilken, R. Holzwarth, and T. Kippenberg, "Optical frequency comb generation from a monolithic microresonator," Nature **450**, 1214–1217 (2007).
4. S. Coen, H. G. Randle, T. Sylvestre, and M. Erkintalo, "Modeling of octave-spanning Kerr frequency combs using a generalized mean-field Lugiato–Lefever model," Opt. Lett. **38**, 37–39 (2013).
5. T. Herr, V. Brasch, J. D. Jost, C. Y. Wang, N. M. Kondratiev, M. L. Gorodetsky, and T. J. Kippenberg, "Temporal solitons in optical microresonators," Nat. Photonics **8**, 145–152 (2014).
6. X. Xue, Y. Xuan, Y. Liu, P.-H. Wang, S. Chen, J. Wang, D. E. Leaird, M. Qi, and A. M. Weiner, "Mode-locked dark pulse Kerr combs in normal-dispersion microresonators," Nat. Photonics **9**, 594–600 (2015).
7. S. Ramelow, A. Farsi, S. Clemmen, J. S. Levy, A. R. Johnson, Y. Okawachi, M. R. E. Lamont, M. Lipson, and A. L. Gaeta, "Strong polarization mode coupling in microresonators," Opt. Lett. **39**, 5134–5137 (2014).
8. K. J. Vahala, "Optical microcavities," Nature **424**, 839–846 (2003).
9. J. Roslund, R. M. de Araújo, S. Jiang, C. Fabre, and N. Treps, "Wavelength-multiplexed quantum networks with ultrafast frequency combs," Nat. Photonics **8**, 109–112 (2014).
10. C.-H. Li, A. J. Benedick, P. Fendel, A. G. Glenday, F. X. Kärtner, D. F. Phillips, D. Sasselov, A. Szentgyorgyi, and R. L. Walsworth, "A laser frequency comb that enables radial velocity measurements with a precision of 1 cm s^{-1}," Nature **452**, 610–612 (2008).
11. Y. K. Chembo and C. R. Menyuk, "Spatiotemporal Lugiato–Lefever formalism for Kerr-comb generation in whispering-gallery-mode resonators," Phys. Rev. A **87**, 053852 (2013).
12. C. Godey, I. V. Balakireva, A. Coillet, and Y. K. Chembo, "Stability analysis of the spatiotemporal Lugiato-Lefever model for Kerr optical frequency combs in the anomalous and normal dispersion regimes," Phys. Rev. A **89**, 063814 (2014).
13. A. B. Matsko, A. A. Savchenkov, W. Liang, V. S. Ilchenko, D. Seidel, and L. Maleki, "Mode-locked Kerr frequency combs," Opt. Lett. **36**, 2845–2847 (2011).
14. J. A. Jaramillo-Villegas, X. Xue, P.-H. Wang, D. E. Leaird, and A. M. Weiner, "Deterministic single soliton generation and compression in microring resonators avoiding the chaotic region," Opt. Express **23**, 9618–9626 (2015).
15. P. Parra-Rivas, D. Gomila, M. A. Matas, S. Coen, and L. Gelens, "Dynamics of localized and patterned structures in the Lugiato-Lefever equation determine the stability and shape of optical frequency combs," Phys. Rev. A **89**, 043813 (2014).
16. W. H. Renninger and P. T. Rakichr, "Closed-form solutions and scaling laws for Kerr frequency combs," Sci. Rep. **6**, 24742 (2016).
17. G. D'Aguanno and C. R. Menyuk, "Nonlinear mode coupling in whispering-gallery-mode resonators," Phys. Rev. A **93**, 043820 (2016).
18. P. F. Byrd and M. D. Friedman, *Handbook of Elliptic Integrals for Engineers and Scientists* (Springer-Verlag, 1971).
19. I. V. Barashenkov and Y. S. Smirnov, "Existence and stability chart for the ac-driven, damped nonlinear Schrödinger solitons," Phys. Rev. E **54**, 5707–5725 (1996).
20. J. A. Fleck, J. R. Morris, and M. D. Feit, "Time-dependent propagation of high energy laser beams through the atmosphere," Appl. Phys. **10**, 129–160 (1976).
21. N. Akhmediev, A. Ankiewicz, J. Soto-Crespo, and J. M. Dudley, "Universal triangular spectra in parametrically-driven systems," Phys. Lett. A **375**, 775–779 (2011).